nature materials

Article

https://doi.org/10.1038/s41563-026-02659-7

High-Chern-number orbital magnetism in twisted rhombohedral graphene

Received: 13 December 2025

Accepted: 4 June 2026

Published online: 03 July 2026

Check for updates

Xirui Wang[1,6] ✉, L. Antonio Benítez[1,6] ✉, Skandaprasad Rao[1], Võ Tiến Phong[2,3], Wai In Chu[1], Kenji Watanabe[4], Takashi Taniguchi[5], Cyprian Lewandowski[2,3] & Pablo Jarillo-Herrero[1] ✉

Realizing Chern insulators with Chern numbers >1 remains a major goal in quantum materials research. Such platforms promise multichannel dissipationless chiral transport and access to correlated phases beyond the conventional $C = 1$ paradigm. We discover high-Chern-number orbital magnets in twisted monolayer–multilayer rhombohedral graphene, denoted $(1 + n)$ with $n = 3$, 4 and 5. Magnetotransport measurements show pronounced anomalous Hall effects at one and three electrons per moiré unit cell when they are polarized away from the moiré interface. Across these systems, we observe a clear topological hierarchy $C = n$, revealed by Středa trajectories and quantized Hall resistance, supported by self-consistent mean-field calculations. Moreover, we realize both electrical and magnetic switching of the high-Chern-number states by flipping the valley polarization. These results establish a tunable hierarchy of orbital Chern magnets in twisted rhombohedral graphene, offering systematic control of Chern number and topology through layer engineering in pristine graphene moiré systems.

Quantized Hall conductance at zero magnetic field arises when the Berry curvature integrated over the Brillouin zone yields a non-zero, integer-valued Chern number C. This bulk topological invariant guarantees the existence of chiral edge states, which in turn produce conductance quantized in C multiples of the conductance quantum. The resulting phase is known as a Chern insulator. Realizing Chern insulators beyond the conventional $C = 1$ regime opens access to topological phases with multiple co-propagating chiral edge modes, providing a direct route to multichannel, low-dissipation transport. Moreover, high-Chern-number systems are predicted to host a hierarchy of exotic fractional and non-Abelian excitations[1–8], which emerge from the interplay between strong correlations and topology, and are central to the pursuit of fault-tolerant topological quantum computation[9]. Motivated by this, magnetic topological insulators have shown that C can be tuned by magnetic doping or layer stacking, thereby establishing a practical design rule for realizing higher-order quantum anomalous Hall states[10].

In parallel, van der Waals heterostructures offer an exciting and versatile platform, with rhombohedral graphene being a particularly promising material candidate because its valley Chern number increases systematically with the number of layers[11–15]. Moreover, theoretical studies predict that the interlayer hybridization between two twisted rhombohedral multilayers enables the design of Chern bands with tunable topology via displacement field and twist angle, and allows the Chern number to be selected by appropriate layer combinations[16–18]. This approach provides a powerful route to design and control topological band structures, yet experimental realizations of such high-Chern-number moiré systems have only recently begun to emerge[19,20]. Importantly, these systems can go beyond the graphene–hexagonal boron nitride (hBN) moiré paradigm, where the broken inversion symmetry in hBN has a strong influence on the electronic properties of rhombohedral graphene but the exact mechanism remains incompletely understood[21].

[1]Department of Physics, Massachusetts Institute of Technology, Cambridge, MA, USA. [2]Department of Physics, Florida State University, Tallahassee, FL, USA. [3]National High Magnetic Field Laboratory, Tallahassee, FL, USA. [4]Research Center for Electronic and Optical Materials, National Institute for Materials Science, Tsukuba, Japan. [5]Research Center for Materials Nanoarchitectonics, National Institute for Materials Science, Tsukuba, Japan. [6]These authors contributed equally: Xirui Wang, L. Antonio Benítez. ✉e-mail: xrwang@mit.edu; lbenitez@mit.edu; pjarillo@mit.edu

https://doi.org/10.1038/s41563-026-02659-7

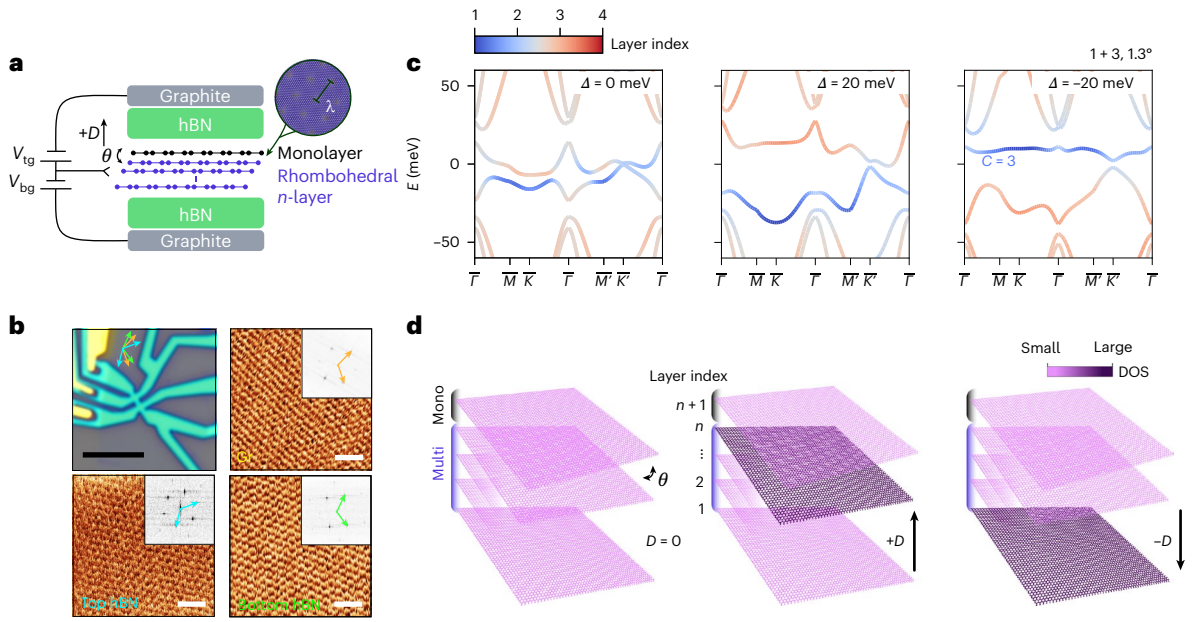

Fig. 1 | Device structure, moiré characterization and band structure calculations in twisted (1 + *n*) systems. a, Schematic of a twisted (1 + *n*) heterostructure, consisting of a monolayer graphene placed on an *n*-layer rhombohedral graphene with a twist angle θ, forming a moiré superlattice of wavelength λ. Top and bottom graphite gates enable independent control of carrier density *n* and displacement field *D*. **b**, Optical micrograph (top left) of a typical device used in this study, and LFM images of graphene (Gr) and top and bottom hBN lattices. The Fourier transform insets reveal the threefold or sixfold symmetry of the atomic lattices, with armchair directions indicated. Scale bars, 5 µm (optical image) and 1 nm (LFM images). **c**, Single-particle band structures of twisted (1 + 3) graphene at $\theta = 1.3°$ at interlayer potential differences Δ of 0, 20 and −20 meV. At $\Delta = -20$ meV, the first conduction band has $C = 3$. The colour represents layer polarization, with 4-red (1-blue) indicating charge localization on the monolayer (multilayer away from moiré interface) side. **d**, Schematic illustration of the evolution of layer polarization with *D*, showing electronic states localized near the moiré interface for $D > 0$ and shifted toward the bottom multilayer surface for $D < 0$. DOS, density of states.

In this work, we engineer a family of twisted monolayer–multilayer rhombohedral graphene (multi-RhG) structures, denoted (1 + *n*), to systematically study how the Chern number evolves as we increase the number of layers. By applying a small twist angle between monolayer and multi-RhG flakes from the same parent crystal, we create a well-defined moiré potential at the interface, enabling controlled exploration and engineering of topological band structures.

Band structure evolution with displacement field

The device schematic and an optical image of a representative device are shown in Fig. 1a,b. The device consists of multi-RhG with a monolayer of graphene (Gr) placed on top, forming a twist angle θ and thereby generating a moiré pattern characterized by moiré wavelength λ. We encapsulate the (1 + *n*) stack with hBN dielectrics, and intentionally misalign them with the graphene lattice to prevent the formation of secondary moiré structures. To this end, we perform lateral force microscopy (LFM) with atomic resolution on both the graphene and hBN flakes. For example, the graphene is misaligned by approximately 30° and 20° relative to the top and bottom hBN, respectively, as shown in Fig. 1b for a twisted (1 + 3) device. Outside the hBN layers, we use top and bottom graphite gates to independently control the displacement field *D* and carrier density *n*. We confirm the rhombohedral stacking order of the multilayer graphene by Raman mapping (Methods and Supplementary Fig. 6), before patterning the stack into a Hall-bar geometry for measuring the longitudinal (R_{xx}) and transverse (R_{yx}) resistances.

According to the single-particle band structure calculations in Fig. 1c, in the absence of a perpendicular displacement field *D*, the low-energy states of the (1 + *n*) system are intrinsically layer-unpolarized. The monolayer graphene is labelled as layer *n* + 1, and the layer index of the multi-RhG stack is denoted by 1, 2,..., *n* (*n* = 3, 4 or 5). For $\Delta = -20$ meV ($D < 0$), the first conduction band flattens and becomes nearly fully polarized toward the bottom layer of the multi-RhG, while carrying a non-trivial Chern number ($C \neq 0$). The calculation in Fig. 1c corresponds to a (1 + 3) system with a twist angle of 1.3°, although a similar behaviour occurs for (1 + 3), (1 + 4) and (1 + 5) structures, predicting a Chern number of 3, 4 and 5 at moderate negative displacement fields, respectively (Supplementary Figs. 1–4). The strong electronic interactions due to the flatness of the conduction band are expected to split the band and generate a cascade of correlated phases (Supplementary Section I(C)). At $\Delta = 20$ meV ($D > 0$), the first conduction band wave function becomes polarized toward the moiré interface. The pronounced band dispersion around the $\bar{\Gamma}$ point indicates that the kinetic energy dominates, thereby suppressing electron–electron correlation effects. By varying *D*, one can thus continuously drive the system between distinct electronic configurations, ranging from flat, layer-polarized bands with non-trivial topology and strong interaction effects, to more dispersive, weakly correlated regimes. Figure 1d schematically illustrates this evolution, highlighting the position of the wave functions either close to the moiré interface for $D > 0$ or further from it for $D < 0$. In our calculations, we treat Δ only as a proxy for *D* that is input into the non-interacting continuum Hamiltonian, while an exact mapping between the two would require a self-consistent electrostatic calculation. The relation between Δ and *D* is explained in Supplementary Section I(D).

High-Chern-number quantum anomalous Hall effect in twisted (1 + *n*) graphene

To reveal the electronic behaviour of the (1 + *n*) systems, Fig. 2 presents R_{xx} and R_{yx} maps as functions of the filling factor *ν* and the displacement field *D*, for *n* = 3, 4 and 5 (information and images of all the devices in this study are shown in Extended Data Table 1 and Extended Data Fig. 1). Throughout this work, R_{xx} and R_{yx} denote the

https://doi.org/10.1038/s41563-026-02659-7

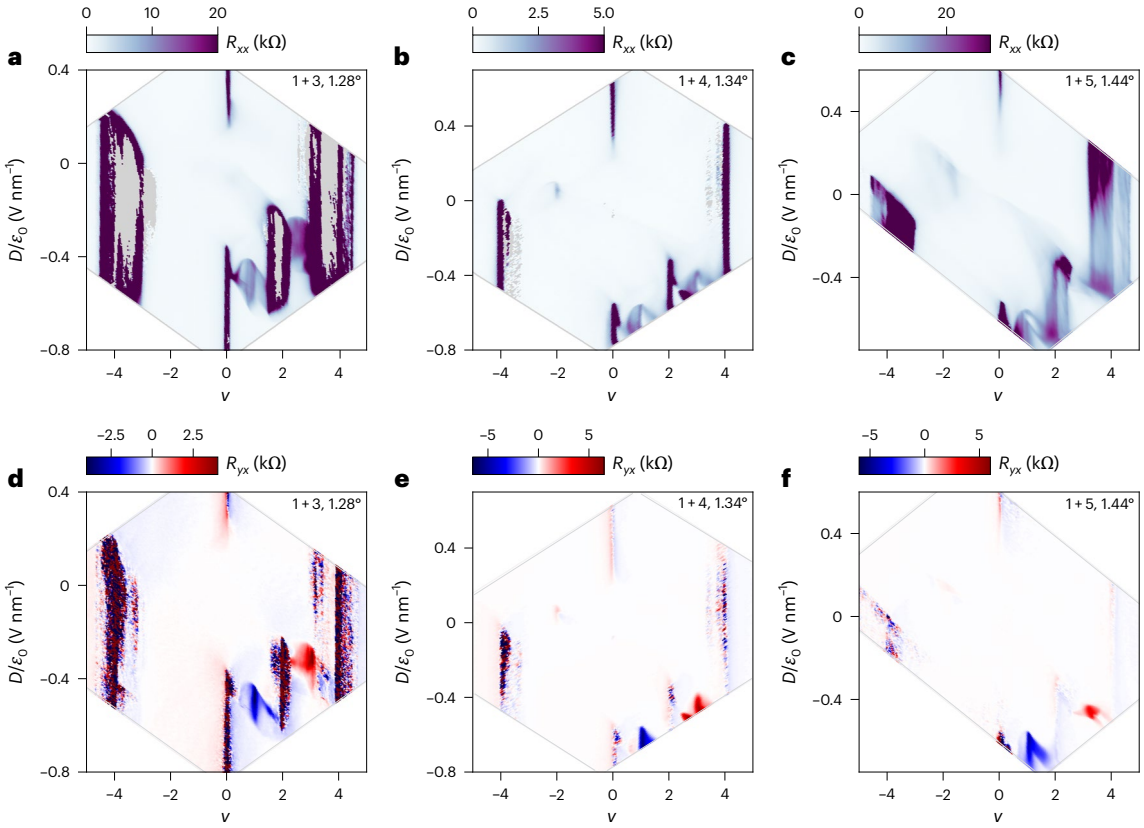

Fig. 2 | Longitudinal and transverse resistance maps of (1 + *n*) systems. **a**–**c**, Longitudinal resistance R_{xx} as a function of filling factor ν and displacement field D/ε_0 for (1 + 3) (**a**), (1 + 4) (**b**) and (1 + 5) (**c**) devices with twist angles of 1.28°, 1.34° and 1.44°, respectively. **d**–**f**, Corresponding dual-gate maps of transverse resistance R_{yx} for the same devices: (1 + 3) (**d**), (1 + 4) (**e**) and (1 + 5) (**f**) with twist angles of 1.28°, 1.34° and 1.44°, respectively. Data were taken at out-of-plane magnetic field B = 0.1 T, 0.15 T and 0.06 T for (1 + 3), (1 + 4) and (1 + 5) devices, respectively, with R_{xx} data symmetrized and R_{yx} antisymmetrized with respect to B. All data were taken at T = 0.3 K.

symmetrized and antisymmetrized components of the raw resistance data with respect to magnetic field, unless otherwise specified. R_{xx} exhibits insulating behaviour at full fillings of conduction and valence bands, reflecting the band insulator formed from the moiré band folding. Near charge neutrality, the system develops a gap as D increases, while on the hole side, R_{xx} remains metallic for all D, consistent with our band structure calculations (Fig. 1c). On the electron side, and particularly for negative D which corresponds to states away from the moiré interface, the R_{xx} maps display pronounced resistive peaks close to integer fillings ν = 1, 2 and 3, indicating tunable symmetry breaking and strong correlation effects. The corresponding R_{yx} maps (Fig. 2d–f) show clear R_{yx} hot spots near ν = 1 and ν = 3 for D < 0. Notably, the hot spot near ν = 1 is highly reproducible across the different (1 + n) systems. Around ν = 3 for the (1 + 3) device, R_{yx} exhibits sign reversals as either D or ν is tuned, indicating a doping- and displacement-field-controlled reversal of the sign of the Berry curvature, which will be discussed later on in detail.

To gain further insight into the R_{yx} hot spots, Fig. 3a–c presents detailed maps of R_{yx} for electron doping and D < 0. To verify their magnetic character, Fig. 3d–f shows R_{xx} and R_{yx} as functions of the out-of-plane magnetic field B at selected values of ν and D. At $\nu \approx 1$, the (1 + 3), (1 + 4) and (1 + 5) devices exhibit similar responses with prominent anomalous Hall signals, and also show hysteresis as B is scanned forward and backward. In the (1 + 4) and (1 + 5) devices, R_{yx} develop quantized plateaus corresponding to C = 4 and C = 5, respectively, indicative of the high-Chern-number quantum anomalous Hall state. A minimal R_{xx} of 0.2 kΩ is reached for the (1 + 4) device at quantization. Detailed measurements of the (1 + 5) device reveal that the quantization extends from D = −0.63 V nm^{-1} to −0.57 V nm^{-1} at ν = 1.0, and a minimal R_{xx} of 3.5 kΩ is reached (Supplementary Fig. 9). The achieved quantized R_{yx} is repeatable across multiple thermal cycles (Supplementary Fig. 9).

Besides quantization at C = 4 observed at ν = 1, R_{yx} of around 9.7 kΩ is observed at ν = 2.73 in the (1 + 4) device, suggesting a Chern state with smaller Chern number. In the (1 + 5) device, we observe R_{yx} hot spots between ν = 1 and ν = 2 that disperse with both ν and D, resembling features previously reported in rhombohedral graphene aligned with hBN[22].

Electrical and magnetic switching of high-Chern-number orbital magnets

To reveal the underlying band topology, we performed measurements at higher magnetic fields. In general, the Hall resistance plateau of an incompressible Chern insulator follows the dispersion $C = \frac{h}{e}\frac{\partial n}{\partial B}$ according to the Středa relation[23], which links the change in carrier density with magnetic field to the Chern number C. In the twisted (1 + 3) device, the Hall plateau at ν = 1 shifts with magnetic field with a slope corresponding to C = 3 as shown in Fig. 4a (in which the dotted line is a guide to the eye). A linecut along this C = 3 trajectory is presented in Extended Data Fig. 2j, showing that R_{yx} begins to saturate near 4 T at a value close to $|R_{yx}| = h/3e^2$, with the measured value slightly higher. The fitting of the dispersion of R_{xx} minima as a function of B also yields a Chern slope of 3 (Extended Data Fig. 2h), consistent with C = 3 predicted by our calculations (Fig. 1c). This observation indicates that electrons are polarized into a single valley as a result of strong electron–electron interactions. Another (1 + 3) device exhibiting quantized R_{yx} around ν = 3 near zero B is shown in Extended Data Fig. 2a–c. In addition to the integer fillings, we also observe an R_{yx} hot spot emerging

https://doi.org/10.1038/s41563-026-02659-7

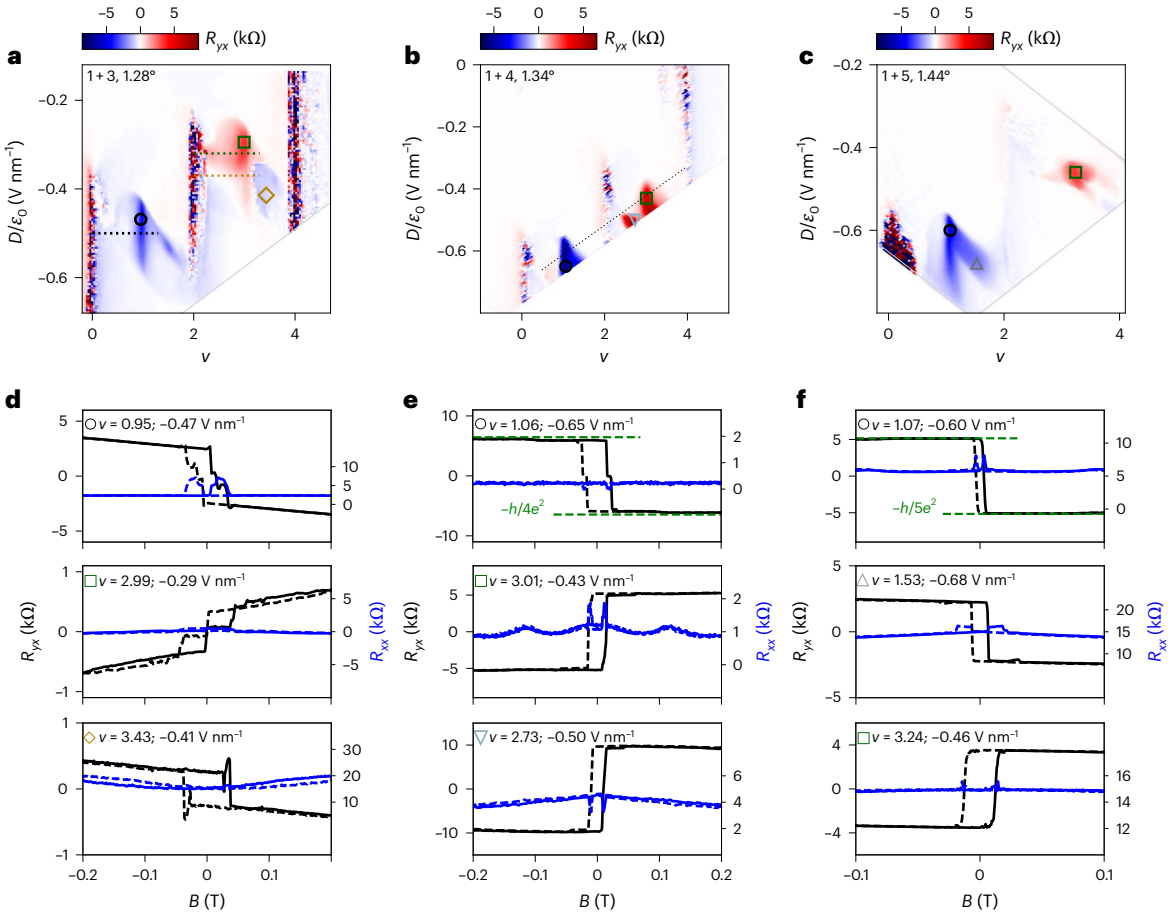

Fig. 3 | Anomalous Hall and high-Chern-number quantum anomalous Hall effects. a–**c**, Zoomed-in dual-gate maps of R_{yx} as a function of ν and D/ε_0 for (1 + 3) (**a**), (1 + 4) (**b**) and (1 + 5) (**c**) devices with twist angles of 1.28°, 1.34° and 1.44°, respectively. **d**–**f**, R_{yx} (antisymmetrized, black) and R_{xx} (symmetrized, blue) measured as a function of B for selected values of ν and D/ε_0, which are labelled with corresponding markers in **a**–**c**. Solid (dashed) lines denote forward (backward) B sweeps. All data were taken at T = 0.3 K.

near $\nu = 1.5$, following a dispersion consistent with a Chern number $C = 2$ (Fig. 4a), pointing toward the possibility of exotic correlated phases such as a topological charge density wave, which combines broken translational symmetry with non-trivial topology[24,25]. Although a quantitative Středa analysis of R_{xx} near $\nu = 1.5$ is challenging in the current sample due to the proximity to the $\nu = 2$ correlation peak, this observation highlights the system as an intriguing platform for future exploration of interaction-driven phases.

In the (1 + 4) device, besides quantization at zero field, linear fitting of the dispersion of R_{yx} maxima and R_{xx} minima yields a Středa slope of $C = 4$ from $\nu = 1$ (Fig. 4b and Extended Data Fig. 3m), agreeing with the theoretical prediction (Supplementary Figs. 2 and 4b). At $\nu = 3$, as shown in Fig. 4e, the R_{yx} hot spot disperses along $C = -4$, indicating that the electrons now occupy the opposite valley compared to $\nu = 1$. In the (1 + 5) device, we observe the R_{yx} dispersion emanating from $\nu = 1$ with a slope corresponding to $C = 5$, as shown in Fig. 4c, in line with the Chern slope extracted from the dispersion of the R_{xx} minima (Extended Data Fig. 4i). At magnetic fields above 0.5 T in Fig. 4c, an additional dispersing feature appears, which probably originates from conventional Landau-level formation. Another R_{yx} hot spot dispersing from $\nu \approx 1.5$ corresponds to the hot-spot region between $\nu = 1$ and $\nu = 2$ observed in Figs. 2f and 3c. The Arrhenius fitting yields a thermal activation gap of 19.4 K for the (1 + 4) device (Extended Data Fig. 3c) and 18.3 K for the (1 + 5) device (Extended Data Fig. 4j). We note that incorporating electron–electron interactions within a self-consistent Hartree–Fock framework yields a spin-valley-polarized state preserving the same topological character as in the single-particle description (Fig. 4d and Supplementary Fig. 5). The calculated band structure also reveals that the electronic states are localized in layers distant from the moiré interface (Supplementary Fig. 4), similar to the behaviour predicted in the twisted (1 + 3) device as illustrated in Fig. 1c,d.

Having demonstrated that the twisted (1 + n) system exhibits a $C = n$ hierarchy, we now illustrate the electrical switching of the high-Chern magnetization. As shown in Fig. 4f, when we sweep the carrier density in the forward direction from $\nu = 1$, R_{yx} switches sign, and a similar behaviour is observed at around $\nu = 3$ in twisted (1 + 3) and (1 + 4) samples (Fig. 3a and Extended Data Figs. 2e and 3j). Given the small spin magnetization in moiré systems, we attribute the doping-induced R_{yx} sign switching to competition between bulk and edge orbital currents, a mechanism previously invoked to explain electrical magnetization switching in moiré graphene systems[26–29]. The bulk contribution comes from self-rotation of the wave packet which evolves within the band and is not directly probed by transport, while the edge contribution is from chiral edge currents when the Fermi level lies within a Chern gap and can be measured through transport. In a single valley, bulk and edge magnetization are opposite in sign[26–29].

Since K and K' valleys have opposite Berry curvature, a flip of the R_{yx} sign corresponds to the change of polarization between the two valleys. We examine three representative linecuts with different sequences of R_{yx} sign reversals using the schematic in Fig. 4g. The corresponding examples are denoted as linecuts in the dual-gate map of the (1 + 3) device (Fig. 3a). As the doping evolves from $\nu = 0$ or 2 towards $\nu = 1$ or 3, R_{yx} either stays negative (black line), positive (green line) or

https://doi.org/10.1038/s41563-026-02659-7

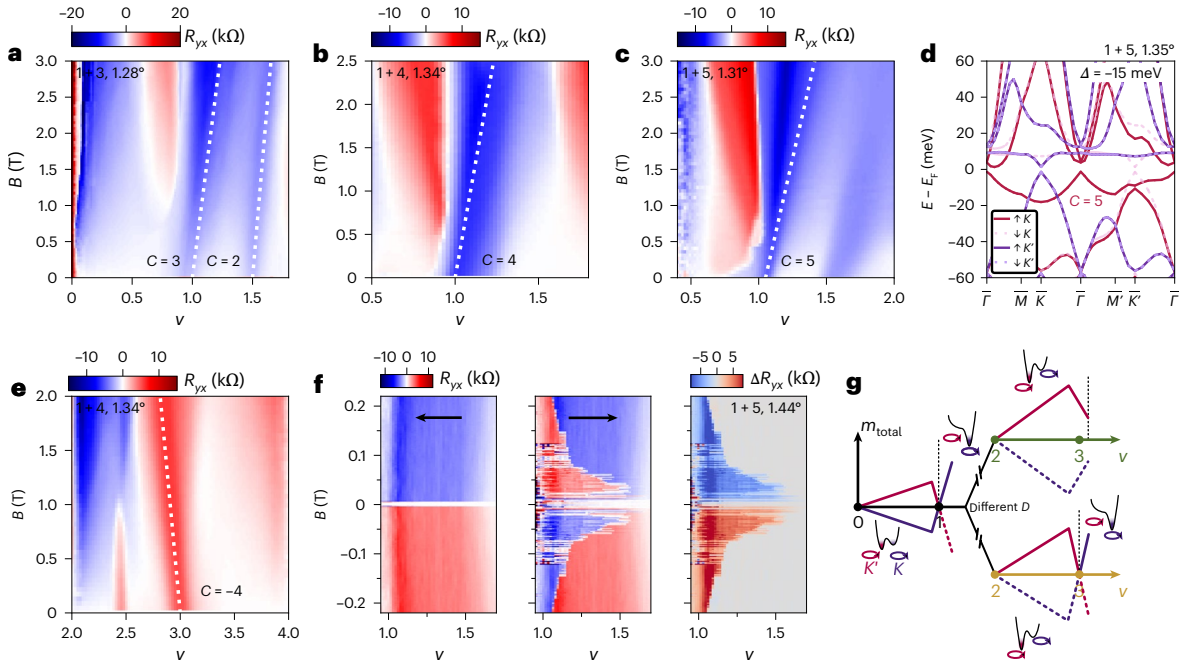

Fig. 4 | Electrical and magnetic switching of high-Chern-number orbital magnets. **a**–**c**,**e**, R_{yx} as a function of ν and B for the (1 + 3) device at $D/\varepsilon_0 = -0.53$ V nm^{-1} (**a**), and for the (1 + 4) device (**b**,**e**) and the (1 + 5) device at $D/\varepsilon_0 = -0.66$ V nm^{-1} (**c**), with twist angles of 1.28°, 1.34° and 1.31°, respectively. Due to the gate limit, **b** and **e** were taken at a constant top-gate voltage. The corresponding linecut is noted with a dashed line in Fig. 3b. The dotted lines which correspond to the noted Chern numbers are drawn as a guide to the eye. **a**–**c**,**e** were taken at $T = 0.3$ K. **d**, Hartree–Fock calculated band structure of 1.35°-(1 + 5) graphene. E_F, Fermi energy. **f**, Doping-induced magnetization switching in the 1.44°-(1 + 5) device at $D/\varepsilon_0 = -0.64$ V nm^{-1}: ν scanned backward (left), forward (middle), and the difference between forward and backward scans (right). $T = 0.05$ K. **g**, Schematic of doping-induced valley polarization switching. Red (purple) solid lines denote K' (K) valley occupied, and dashed lines denote unoccupied valleys. x axis, ν; y axis, total magnetization m_{total} of either valley. The three segments denote linecuts along ν at different displacement fields (linecuts drawn in Fig. 3a with corresponding colours as an example).

changes from positive to negative (yellow line). The total magnetization m_{total} from either K' (red) or K (purple) valley is plotted as a function of doping.

The system tends to minimize the Zeeman energy by aligning the total magnetization with the external magnetic field. When the Fermi level goes across the Chern gap, if the total magnetization of a single valley changes sign, the system tends to switch valley to maintain low Zeeman energy, leading to a reversal of R_{yx} from positive to negative (yellow line). In the quantized (1 + 5) device, this enables electrical switching of the high-Chern quantization, as shown in Extended Data Fig. 4g,h. On the other hand, if the sign of the total magnetization of a single valley remains the same (green line), it results in a continuous evolution of positive R_{yx} without sign reversal. The black line corresponds to the case where the large negative R_{yx} at $\nu = 1$ indicates polarization into the K valley, while the small negative R_{yx} at $\nu < 1$ reflects nearly equal valley polarization, probably due to the large energy barrier for single-valley polarization at lower doping (Fig. 4g).

The above framework also explains the field-dependent sign reversal, where a high magnetic field tilts the energy landscape between K and K' valleys, so that a sign reversal as function of doping can happen which otherwise does not occur at small B, as shown in Fig. 4a–c. Doping-induced valley switching is accompanied by pronounced hysteresis as carrier density is swept forward and backward (Fig. 4f and Supplementary Fig. 13). This indicates that the valley switching occurs via a first-order phase transition probably due to domain-wall pinning between regions harbouring opposite valley polarization. The divergence of the coercive magnetic field around $\nu = 1$ or 3 further suggests a minimal energy splitting between the K and K' valleys[28]. We note that while the above discussion provides a possible picture of the electrical magnetization switching mechanism, local imaging methods will enable a more definitive identification of its microscopic origin.

Conclusion

Our experiments establish the twisted (1 + n) family of graphene moiré systems as a promising platform for engineering high-Chern-number bands through controlled combinations of rhombohedral layer number and twist angle, with high reproducibility across multiple devices (Extended Data Figs. 2–4 and Supplementary Fig. 9). A key and unique aspect of our work is that we propose and observe a systematic and predictable approach to engineering high-Chern-number orbital magnets in graphene moiré systems. Although recent studies have explored individual moiré structures, often accompanied by theoretical descriptions developed independently for each specific system[19,20,30], our work reveals a simple and unified design principle: for the (1 + n) family, the isolated Chern band carries Chern number $C = n$, giving rise to anomalous Hall states at fillings of one and three electrons per moiré unit cell. Despite the substantial differences among tri-, tetra- and penta-layer rhombohedral graphene, their behaviour when interfaced with monolayer graphene is remarkably similar: all exhibit robust, and in some cases quantized, anomalous Hall effects when electrons localize in the layer furthest from the moiré interface. Beyond the systematic Chern hierarchy, the observation of electrically switchable high-Chern quantization further highlights the robustness of this design principle and opens new opportunities for topological electronics.

It is instructive to compare our results with multi-RhG aligned with hBN. In that case, alignment produces an isolated flat Chern band with $C = 1$, independent of layer number, in contrast to our twisted (1 + n) systems in which the Chern number scales with the rhombohedral block thickness. We note that, in our case, the mono/multi-RhG twist interface provides a well-defined moiré potential free from the sublattice ambiguity of hBN, allowing a straightforward comparison with theoretical calculations. In fact, the observed layer-dependent Chern hierarchy is in agreement with predictions of single-particle band model calculations, which remain qualitatively unchanged after introduction of

Coulomb interactions at a mean-field level. These findings highlight the distinct roles of moiré potential and interlayer hybridization in determining topological band structures in graphene-based systems.

Moving forward, it should prove promising to explore smaller twist angles in $(1+n)$ systems, where the flatter band can promote a correlation effect favourable for fractional states to emerge (Supplementary Fig. 4). Future extensions to multilayer configurations such as (2 + 3), (2 + 4) or (2 + 5) rhombohedral graphene will be particularly intriguing because bilayer or thicker rhombohedral graphene can host isolated flat bands tunable by displacement field, providing a promising route to further enhance correlations in the topological bands[18]. These systems could offer an ideal setting for realizing fractional states in high-Chern-number bands. Furthermore, given the plethora of unconventional superconductivity observed in rhombohedral graphene[31–37], creating lateral junctions to couple high-Chern-number insulators with superconductivity could open new opportunities for non-Abelian statistics and topological superconductivity[38,39].

Note added in proof: During the preparation of this paper, we became aware of a related study on twisted (1 + 5) rhombohedral graphene[30].

Online content

Any methods, additional references, Nature Portfolio reporting summaries, source data, extended data, supplementary information, acknowledgements, peer review information; details of author contributions and competing interests; and statements of data and code availability are available at https://doi.org/10.1038/s41563-026-02659-7.

References

1. Wang, Y.-F., Yao, H., Gong, C.-D. & Sheng, D. N. Fractional quantum Hall effect in topological flat bands with Chern number two. *Phys. Rev. B* **86**, 201101 (2012).
2. Barkeshli, M. & Qi, X.-L. Topological nematic states and non-Abelian lattice dislocations. *Phys. Rev. X* **2**, 031013 (2012).
3. Liu, Z., Bergholtz, E. J., Fan, H. & Läuchli, A. M. Fractional Chern insulators in topological flat bands with higher Chern number. *Phys. Rev. Lett.* **109**, 186805 (2012).
4. Sterdyniak, A., Repellin, C., Bernevig, B. A. & Regnault, N. Series of Abelian and non-Abelian states in $C>1$ fractional Chern insulators. *Phys. Rev. B* **87**, 205137 (2013).
5. Liu, T., Repellin, C., Bernevig, B. A. & Regnault, N. Fractional Chern insulators beyond Laughlin states. *Phys. Rev. B* **87**, 205136 (2013).
6. Möller, G. & Cooper, N. R. Fractional Chern insulators in Harper–Hofstadter bands with higher Chern number. *Phys. Rev. Lett.* **115**, 126401 (2015).
7. Andrews, B. & Möller, G. Stability of fractional Chern insulators in the effective continuum limit of Harper–Hofstadter bands with Chern number $|C|>1$. *Phys. Rev. B* **97**, 035159 (2018).
8. Andrews, B., Neupert, T. & Möller, G. Stability, phase transitions, and numerical breakdown of fractional Chern insulators in higher Chern bands of the Hofstadter model. *Phys. Rev. B* **104**, 125107 (2021).
9. Nayak, C., Simon, S. H., Stern, A., Freedman, M. & Das Sarma, S. Non-Abelian anyons and topological quantum computation. *Rev. Mod. Phys.* **80**, 1083 (2008).
10. Zhao, Y.-F. et al. Tuning the Chern number in quantum anomalous Hall insulators. *Nature* **588**, 419–423 (2020).
11. Zhou, H. et al. Half- and quarter-metals in rhombohedral trilayer graphene. *Nature* **598**, 429–433 (2021).
12. Han, T. et al. Correlated insulator and Chern insulators in pentalayer rhombohedral-stacked graphene. *Nat. Nanotechnol.* **19**, 181–187 (2024).
13. Liu, K. et al. Spontaneous broken-symmetry insulator and metals in tetralayer rhombohedral graphene. *Nat. Nanotechnol.* **19**, 188–195 (2024).
14. Han, T. et al. Large quantum anomalous Hall effect in spin-orbit proximitized rhombohedral graphene. *Science* **384**, 647–651 (2024).
15. Sha, Y. et al. Observation of a Chern insulator in crystalline ABCA-tetralayer graphene with spin-orbit coupling. *Science* **384**, 414–419 (2024).
16. Ledwith, P. J., Vishwanath, A. & Khalaf, E. Family of ideal Chern flatbands with arbitrary Chern number in chiral twisted graphene multilayers. *Phys. Rev. Lett.* **128**, 176404 (2022).
17. Wang, J. & Liu, Z. Hierarchy of ideal flatbands in chiral twisted multilayer graphene models. *Phys. Rev. Lett.* **128**, 176403 (2022).
18. Phong, V. T. & Lewandowski, C. Coulomb interaction-stabilized isolated narrow bands with Chern numbers $\mathcal{C}>1$ in twisted rhombohedral trilayer-bilayer graphene. Preprint at https://arxiv.org/abs/2505.07981 (2025).
19. Dong, J. et al. Observation of Integer and Fractional Chern insulators in high Chern number flatbands. Preprint at https://arxiv.org/abs/2507.09908 (2025).
20. Wang, W. et al. Programmable quantum anomalous hall insulator in twisted crystalline flatbands. *Phys. Rev. X* **16**, 011015 (2026).
21. Uzan, M. et al. hBN alignment orientation controls moiré strength in rhombohedral graphene. Preprint at https://arxiv.org/abs/2507.20647 (2025).
22. Zheng, J. et al. Switchable Chern insulators and competing quantum phases in rhombohedral graphene moiré superlattices. *Phys. Rev. Lett.* **135**, 136302 (2025).
23. Streda, P. Quantised Hall effect in a two-dimensional periodic potential. *J. Phys. C* **15**, L1299 (1982).
24. Polshyn, H. et al. Topological charge density waves at half-integer filling of a moiré superlattice. *Nat. Phys.* **18**, 42–47 (2022).
25. Xie, Y. et al. Fractional Chern insulators in magic-angle twisted bilayer graphene. *Nature* **600**, 439–443 (2021).
26. Polshyn, H. et al. Electrical switching of magnetic order in an orbital Chern insulator. *Nature* **588**, 66–70 (2020).
27. Zhu, J., Su, J.-J. & MacDonald, A. H. Voltage-controlled magnetic reversal in orbital Chern insulators. *Phys. Rev. Lett.* **125**, 227702 (2020).
28. Tschirhart, C. et al. Imaging orbital ferromagnetism in a moiré Chern insulator. *Science* **372**, 1323–1327 (2021).
29. Grover, S. et al. Chern mosaic and Berry-curvature magnetism in magic-angle graphene. *Nat. Phys.* **18**, 885–892 (2022).
30. Liu, N. et al. Diverse high-Chern-number quantum anomalous Hall insulators in twisted rhombohedral graphene. Preprint at https://arxiv.org/abs/2507.11347 (2025).
31. Seo, J. et al. Family of unconventional superconductivities in crystalline graphene. Preprint at https://arxiv.org/abs/2509.03295 (2025).
32. Kumar, M. et al. Superconductivity from dual-surface carriers in rhombohedral graphene. *Nat. Phys.* **22**, 862–869 (2026).
33. Morissette, E. et al. Superconductivity, anomalous Hall effect, and stripe order in rhombohedral hexalayer graphene. Preprint at https://arxiv.org/abs/2504.05129 (2025).
34. Nguyen, R. Q. et al. A hierarchy of superconductivity and topological charge density wave states in rhombohedral graphene. Preprint at https://arxiv.org/abs/2507.22026 (2025).
35. Deng, J. et al. Superconductivity and ferroelectric orbital magnetism in semimetallic rhombohedral hexalayer graphene. Preprint at https://arxiv.org/abs/2508.15909 (2025).
36. Kumar, M. et al. Pervasive spin-triplet superconductivity in rhombohedral graphene. Preprint at https://arxiv.org/abs/2511.16578 (2025).
37. Guo, Y. et al. Flat band surface state superconductivity in thick rhombohedral graphene. Preprint at https://arxiv.org/abs/2511.17423 (2025).

38. Choi, Y. et al. Superconductivity and quantized anomalous Hall effect in rhombohedral graphene. *Nature* **639**, 342–347 (2025).
39. Röntynen, J. & Ojanen, T. Topological superconductivity and high Chern numbers in 2D ferromagnetic Shiba lattices. *Phys. Rev. Lett.* **114**, 236803 (2015).

Methods

Flake identification

hBN and graphite crystals were exfoliated onto SiO_2 (285–295 nm)/Si substrates. The thickness of hBN flakes was determined by atomic force microscopy (AFM), and the thickness of the 1–5 layers of graphene flakes were identified by optical contrast. The graphene stacking order was identified using an infrared (IR) camera as described in ref. 40, and then mapped with Raman spectroscopy (Renishaw Invia Reflex Micro Raman; wavelength, 532 nm) to confirm the stacking order (Supplementary Fig. 6). Then it is cut by AFM anodic cutting to isolate the rhombohedral stacking pieces as described in ref. 41. The crystallographic axis of rhombohedral graphene and some of the hBNs were identified using LFM.

Transfer processes

We first prepared the bottom stacks. For devices (1 + 3)-3 and (1 + 4)-2 (see device names in Extended Data Table 1), we evaporated PdAu(13 nm)/Ti(2 nm) on SiO_2(285 nm)/Si substrates by thermal evaporation for the bottom electrodes. After heat annealing at 300 °C under a mixture of H_2 and argon gas, we transferred hBN as a bottom-gate dielectric using poly(bisphenol A carbonate) (PC) film on polydimethylsiloxane. For the other devices, an hBN and a graphite flake were sequentially picked up and then released to a SiO_2/Si substrate at 170 °C. After the PC was dissolved, contact-mode AFM was performed at a deflection voltage of 0.1–0.2 V to clean the PC residues. Top stacks fabricated for the (1 + 3)-3 and (1 + 4)-2 devices were made by the sequential pickup of top hBN and twisted monolayer–multilayer graphene. Top stacks for the other devices were made by the sequential pickup of topmost hBN, top graphite, top hBN and twisted monolayer–multilayer graphene. Twisted monolayer–multilayer graphene was picked up with the cut-and-stack method described in ref. 42. The whole stack was then released to the bottom stack at between 110 and 170 °C. During the transfer, we intentionally misalign the graphene from top and bottom hBNs based on the LFM of graphene and the straight edges or the LFM of the hBN.

Post-transfer fabrication

Raman spectroscopy and IR camera were used again to search for any rhombohedral regions that survived the transfer. After the transfer, we sometimes identify three types of regions, corresponding to a rhombohedral flake surviving with the monolayer twisted on top, a rhombohedral flake relaxed to Bernal stacking, and a rhombohedral flake surviving but with the monolayer fully aligned and forming the $(1 + n)$ layers of rhombohedral graphene. They typically show different contrast in the Raman spectroscopy and the IR images (Supplementary Fig. 7), but require a careful comparison between different regions to identify the exact stacking orders, and sometimes require transport measurement to finally confirm the stacking order. After Raman scanning and IR imaging, we identify the stack with an optical microscope and AFM for bubble-free regions. Then the stack was etched into a Hall-bar shape by reactive ion etching. All the contacts (and metal top gates) were deposited with Au/Cr with a thermal evaporator.

LFM measurements

To determine the crystallographic axis, we performed LFM measurements on the rhombohedral graphene flakes and on some of the top and bottom hBN flakes. To avoid the LFM causing any change in the stacking order, we scanned on the Bernal stacking part that is from the same piece of graphite as the rhombohedral graphene. The LFM measurements were performed with an Asylum Research Cypher S atomic force microscope at room temperature. We used an Asyelec-01-R2 tip with a force constant of around 2.8 N m^{-1} and a deflection setpoint of around 2 V.

Transport measurements

The devices were bonded to aluminium wire. The four-probe measurements were done using lock-in amplifiers (SR830 and SR860, SRS), a current preamplifier (1211, DL) and voltage preamplifiers (SR560, SRS; 1201, Ithaco) at frequencies of 17–35 Hz. The gate voltages were applied by source meters (2400 and 2450, Keithley). Devices were measured in a He-3 cryostat (Janis Research) or a dilution fridge (Leiden Cryogenics). All the measurements were done at $T = 0.3$ K unless noted otherwise.

Density calibration

We calculate the carrier density using a parallel-plate capacitor model, $n = \epsilon_0(\epsilon_t V_t/d_t + \epsilon_b V_b/d_b)/e$, where V, ϵ and d denote the gate voltage, dielectric constant and hBN thickness, respectively. The subscripts 't' and 'b' denote the top-gate and bottom-gate parameters. The hBN thicknesses are measured by AFM.

The dielectric constant can then be determined by tracking Landau-level features in dual-gate maps at finite B. The change in carrier density between adjacent Landau levels corresponds to $\Delta n = geB/h$, where the degeneracy $g = 4$ in the full metal phase. By measuring the spacing in V_t and V_b between adjacent Landau levels, we can fit the density equation above and extract ϵ_t and ϵ_b.

Importantly, we note that the Chern number extracted from the Středa relation, $\Delta n = Ce\Delta B/h$, can be determined by direct comparison with the Landau-level spacings in the full metal phase as described above, without the need to calculate the dielectric constants. Therefore, the inferred hierarchy $C = n$ is robust against variations in density calibration. The uncertainty in the density calibration only affects our estimation of the twist angle, which is calculated using the carrier density at full filling $n_0 = (8/\sqrt{3}a^2)\,\theta^2$, where a is the lattice constant.

Magnetic hysteresis analysis

In this study, we apply standard symmetrization and antisymmetrization procedures to the magnetic hysteresis data, to eliminate mixing between R_{xx} and R_{yx} caused by contact misalignment (b (f) for backward (forward) B sweeps):

$$R_{xx}^{\mathrm{sym,f}}(B) = \frac{R_{xx}^{\mathrm{raw,f}}(B) + R_{xx}^{\mathrm{raw,b}}(-B)}{2}, R_{xx}^{\mathrm{sym,b}}(B) = R_{xx}^{\mathrm{sym,f}}(-B);$$

$$R_{yx}^{\mathrm{antisym,f}}(B) = \frac{R_{yx}^{\mathrm{raw,f}}(B) - R_{yx}^{\mathrm{raw,b}}(-B)}{2}, R_{yx}^{\mathrm{antisym,b}}(B) = -R_{yx}^{\mathrm{antisym,f}}(-B).$$

Středa analysis procedure

The Chern number is obtained from the Středa relation $C = (h/e)\partial n/\partial B$, where the carrier density n is determined from the Landau fan analysis. In practice, because R_{yx} directly reflects the topologically protected Hall response, whereas R_{xx} can be more sensitive to disorder and dissipation[43], we primarily track the dispersing feature in R_{yx} and use R_{xx} as a consistency check.

For the devices where clear dispersing features are observed, we take linecuts on the R_{yx} map along the integer-C trajectory that best follows the prominent dispersing feature and confirm the C number by observing the quantization, as has been done for the (1 + 3) and (1 + 5) devices in the main text.

For the devices that do not reach full quantization, we track the dispersing maxima in R_{yx} within a window of $\Delta\nu = 0.5$ and perform linear fitting to extract the Chern number, which is done for the additional (1 + 3) and (1 + 4) devices in Extended Data Figs. 2g and 3p,q.

Data availability

The experimental data in the study are available at the Harvard Dataverse via https://doi.org/10.7910/DVN/CONZGR.

References

40. Lu, Z. et al. Extended quantum anomalous Hall states in graphene/hBN moiré superlattices. *Nature* **637**, 1090–1095 (2025).
41. Li, H. et al. Electrode-free anodic oxidation nanolithography of low-dimensional materials. *Nano Lett.* **18**, 8011–8015 (2018).

42. Park, J. M., Cao, Y., Watanabe, K., Taniguchi, T. & Jarillo-Herrero, P. Flavour Hund's coupling, Chern gaps and charge diffusivity in moiré graphene. *Nature* **592**, 43–48 (2021).
43. Weis, J. & Von Klitzing, K. Metrology and microscopic picture of the integer quantum Hall effect. *Philos. Trans. R. Soc. A* **369**, 3954–3974 (2011).

Acknowledgements

We thank P. Ledwith and J. M. Park for fruitful discussions, and L.-Q. Xia and C. Collignon for the help with the measurement set-up.

Author contributions

X.W. and L.A.B. conceived of the project. X.W., L.A.B. and S.R. fabricated the devices and performed measurements with the help of W.I.C. V.T.P. performed the theoretical calculations supervised by C.L. K.W. and T.T. grew the hBN crystals. P.J.-H. supervised the project. X.W. and L.A.B. analysed the data and wrote the paper with input from all the other authors.

Funding

This research was supported by the Center for the Advancement of Topological Semimetals, an Energy Frontier Research Center funded by the US Department of Energy Office of Science, through the Ames Laboratory under contract DE-AC02-07CH11358 (measurements and data analysis), the Air Force Office of Scientific Research (AFOSR) grant FA9550-21-1-0319 (characterization), the Office of Naval Research (ONR) grant N000142412440 (device fabrication), the MIT/Microsystems Technology Laboratories Samsung Semiconductor Research Fund, the Gordon and Betty Moore Foundation's EPiQS Initiative through grant GBMF9463, and the Ramon Areces Foundation. This work was performed in part at the Harvard University Center for Nanoscale Systems (CNS), a member of the National Nanotechnology Coordinated Infrastructure Network (NNCI), which is supported by the National Science Foundation under NSF ECCS award number 1541959. This work was carried out in part through the use of MIT.nano's facilities. X.W. acknowledges support from a Mathworks fellowship. L.A.B. gratefully acknowledges the generous support of the Mauricio and Carlota Botton Foundation. K.W. and T.T. acknowledge support from the JSPS KAKENHI (grant numbers 21H05233 and 23H02052), the CREST (JPMJCR24A5), JST and the World Premier International Research Center Initiative (WPI), MEXT, Japan. Numerical calculations were done using the High Performance Compute Cluster of the Research Computing Center (RCC) at Florida State University. V.T.P. and C.L. are supported by start-up funds from Florida State University and the National High Magnetic Field Laboratory. The National High Magnetic Field Laboratory is supported by the National Science Foundation through NSF/DMR-2128556 and the State of Florida.

Competing interests

The authors declare no competing interests.

Additional information

Extended data is available for this paper at https://doi.org/10.1038/s41563-026-02659-7.

Supplementary information The online version contains supplementary material available at https://doi.org/10.1038/s41563-026-02659-7.

Correspondence and requests for materials should be addressed to Xirui Wang, L. Antonio Benítez or Pablo Jarillo-Herrero.

Peer review information *Nature Materials* thanks the anonymous reviewers for their contribution to the peer review of this work.

https://doi.org/10.1038/s41563-026-02659-7

Extended Data Table 1 | Device summary

Device	AHE	Gate	Twist (°)	Best R_{yx} value (kΩ) and quantization percentage	B_c (mT)	ν, D/ε_0 (V/nm) range (>90% quantization)
(1+3)-1	✓	Gr	1.28	2.5 (0 T, 29%) 8.7 (4 T, quantized)	15	ν : 1.23 ~ 1.39, D/ε_0 : −0.53 (4 T)
(1+3)-2	✓	Gr	1.33	6.7 (0 T, 78%)	36	NA
(1+3)-3	✓	Au	1.11 #	8.1 (0 T, 94%)	1	ν : 2.57 ~ 2.79, D/ε_0 : −0.20 ν : 2.61, D/ε_0 : −0.22 ~ −0.19
(1+3)-4	✗	Gr	0.94	NA	NA	NA
(1+3)-5	✗	Gr	0.90	NA	NA	NA
(1+4)-1	✓	Gr	1.34	6.1 (0 T, 95%)	17	ν : 1.04 ~ 1.11, D/ε_0 : −0.65 ν : 1.05, D/ε_0 : −0.65 ~ −0.56 (gate range limited)
(1+4)-2	✓	Au	1.39	2.8 (0 T, 43%) 5.7 (3 T, 87%)	5	NA
(1+4)-3	✓	Gr	1.22	4.8 (0 T, 74%)	19	NA
(1+5)-1	✓	Gr	1.31	4.8 (0 T, 93%)	22	ν : 1.01 ~ 1.04, D/ε_0 : −0.58 ν : 1.01, D/ε_0 : −0.62 ~ −0.57
(1+5)-2	✓	Gr	1.39	4.8 (0 T, 93%)	not measured	ν : 0.74 ~ 1.02, D/ε_0 : −0.73 ν : 1.02, D/ε_0 : −0.74 ~ −0.71
(1+5)-3	✓	Gr	1.44	5.1 (0 T, 99%)	3	ν : 1.01 ~ 1.09, D/ε_0 : −0.61 † ν : 1.02, D/ε_0 : −0.65 ~ −0.57 †

AHE: anomalous Hall effect. #: Assuming an hBN dielectric constant ε_{hBN} = 3 for the device. For the other devices, ε_{hBN} is extracted from Landau fan features. Device (1+5)-3 was obtained by etching the device previously measured as (1+5)-1 and (1+5)-2. B_c denotes the critical field at which R_{yx} crosses zero. †: All other values were measured at 0.3 K, except those marked here, which were measured at 0.05 K.

https://doi.org/10.1038/s41563-026-02659-7

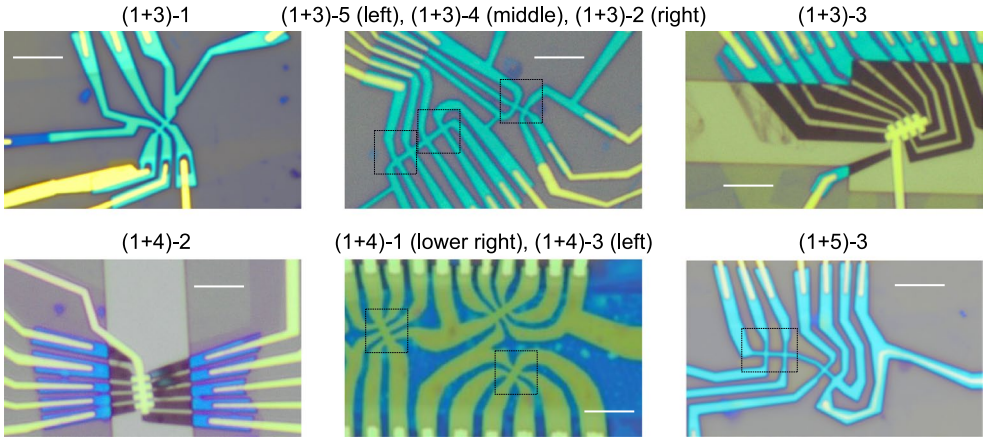

Extended Data Fig. 1 | Optical micrograph of fabricated (1+*n*) graphene devices. Scale bar, 5 μm.

https://doi.org/10.1038/s41563-026-02659-7

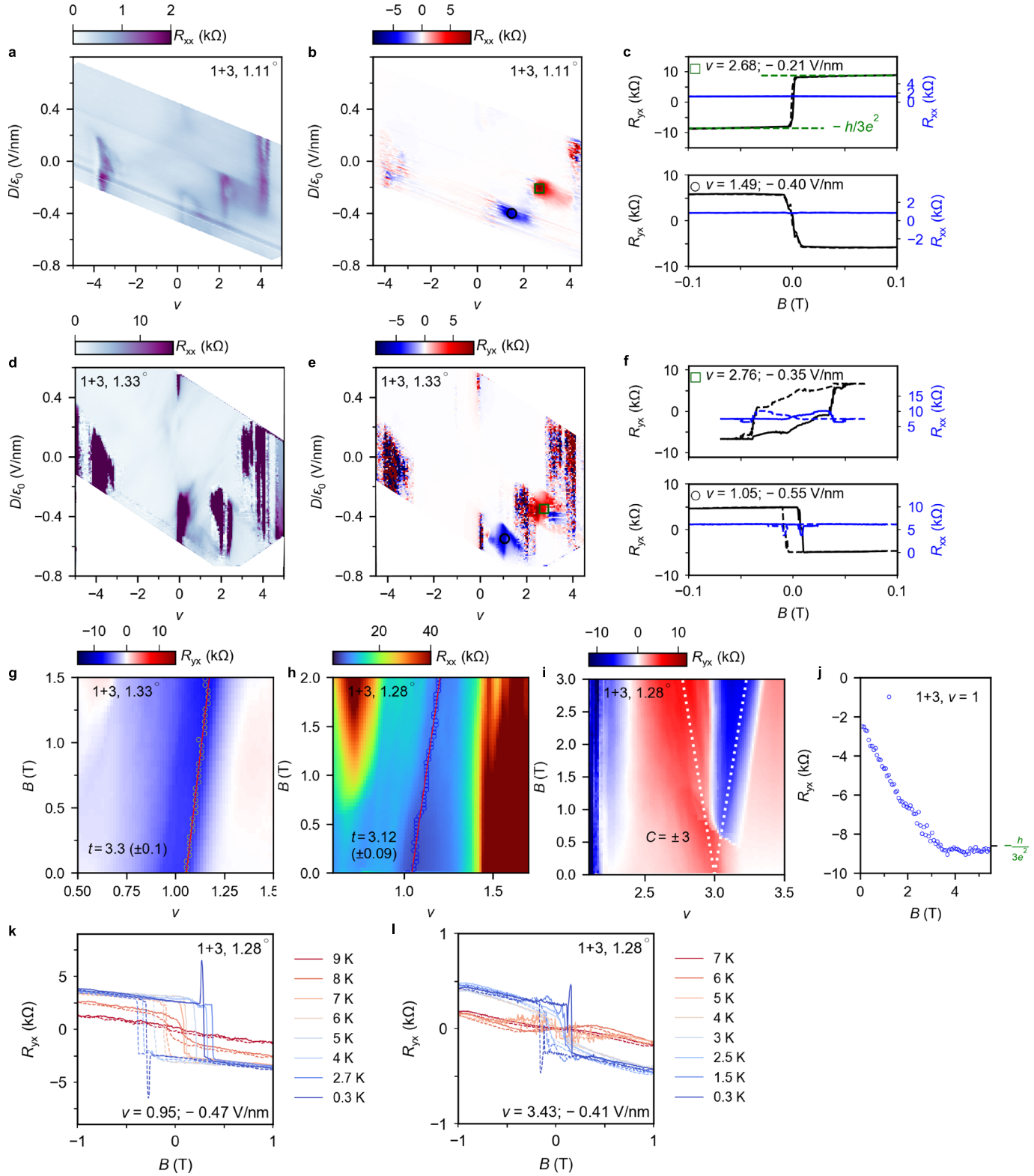

Extended Data Fig. 2 | Additional data of (1+3) graphene devices. a,**b**, Dual-gate maps of R_{xx} and R_{yx} of the 1.11°-(1+3) device. $B = 0.1$ T. **c**, R_{yx} and R_{xx} as a function of B (corresponding points labeled in b). **d**,**e**, Dual-gate maps of R_{xx} and R_{yx} of the 1.33°-(1+3) device. $B = 0.06$ T. **f**, R_{yx} and R_{xx} as a function of B (corresponding points labeled in e). **g**, R_{yx} as a function of ν and B for the 1.33°-(1+3) device. **h**, R_{xx} as a function of ν and B for the 1.28°-(1+3) device. Red solid lines are linear fits to the hollow circles, which mark ν for the local extremum at each B. **i**, R_{yx} as a function of ν and B for the 1.28°-(1+3) device ($D/\varepsilon_0 = -0.29$ V/nm). Dotted lines with denoted Chern numbers are drawn as a guide to the eye. **j**, Linecut in main Fig. 4a along the dotted line from $\nu = 1$. **k**,**l**, R_{yx} measured as a function of B at different temperatures. Solid (dashed) lines denote forward (backward) B sweeps in the hysteretic plots.

https://doi.org/10.1038/s41563-026-02659-7

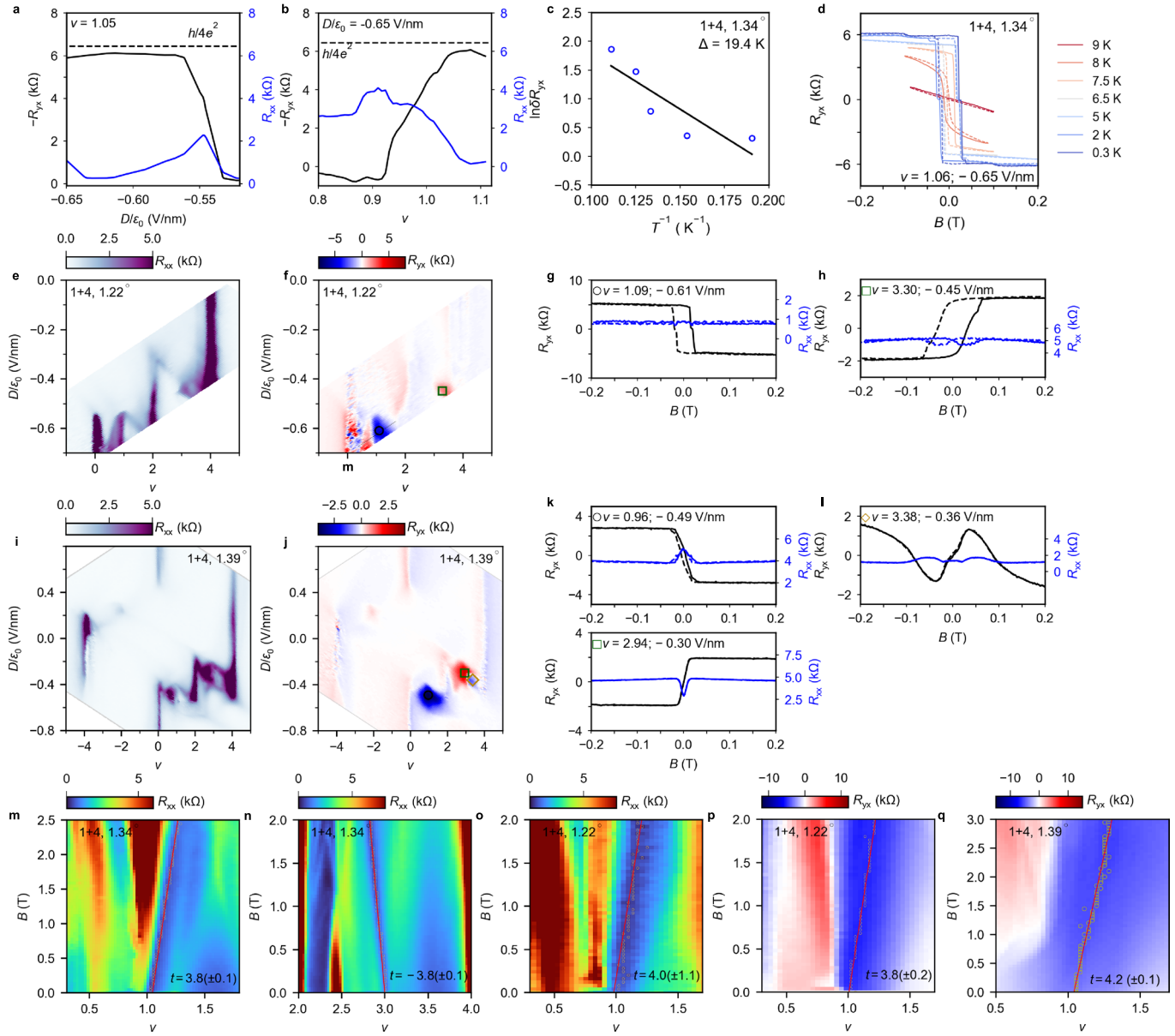

Extended Data Fig. 3 | Additional data of (1+4) graphene devices. a,**b**, Linecuts of R_{xx} and $-R_{yx}$ at fixed ν or D/ε_0 for the 1.34°-(1+4) device. $B = 0.2$ T. **c**, Deviation of R_{yx} from quantization plotted as a function of temperature, extracting a gap size $\Delta = 19.4$ K for the (1+4) device by fitting $\delta R_{yx} = \exp(-\Delta/k_B T)$. **d**, R_{yx} measured as a function of B at different temperatures. **e**,**f**, Dual-gate maps of R_{xx} and R_{yx} of the 1.22°-(1+4) device. $B = 0.2$ T. **g**,**h**, R_{yx} and R_{xx} measured as a function of B (corresponding points labeled in f). **i**,**j**, Dual-gate maps of R_{xx} and R_{yx} of the 1.39°-(1+4) device. $B = 0.2$ T. **k**,**l**, R_{yx} and R_{xx} measured as a function of B (corresponding points labeled in j). **m**,**n**, R_{xx} as a function of ν and B for the 1.34°-(1+4) device. **o**,**p**, R_{xx} and R_{yx} as a function of ν and B for the 1.22°-(1+4) device. **q**, R_{yx} as a function of ν and B for the 1.39°-(1+4) device. In **m** to **q**, red solid lines are linear fits to the hollow circles, which mark ν for the local extremum at each B. Solid (dashed) lines denote forward (backward) sweeps in the hysteretic plots.

https://doi.org/10.1038/s41563-026-02659-7

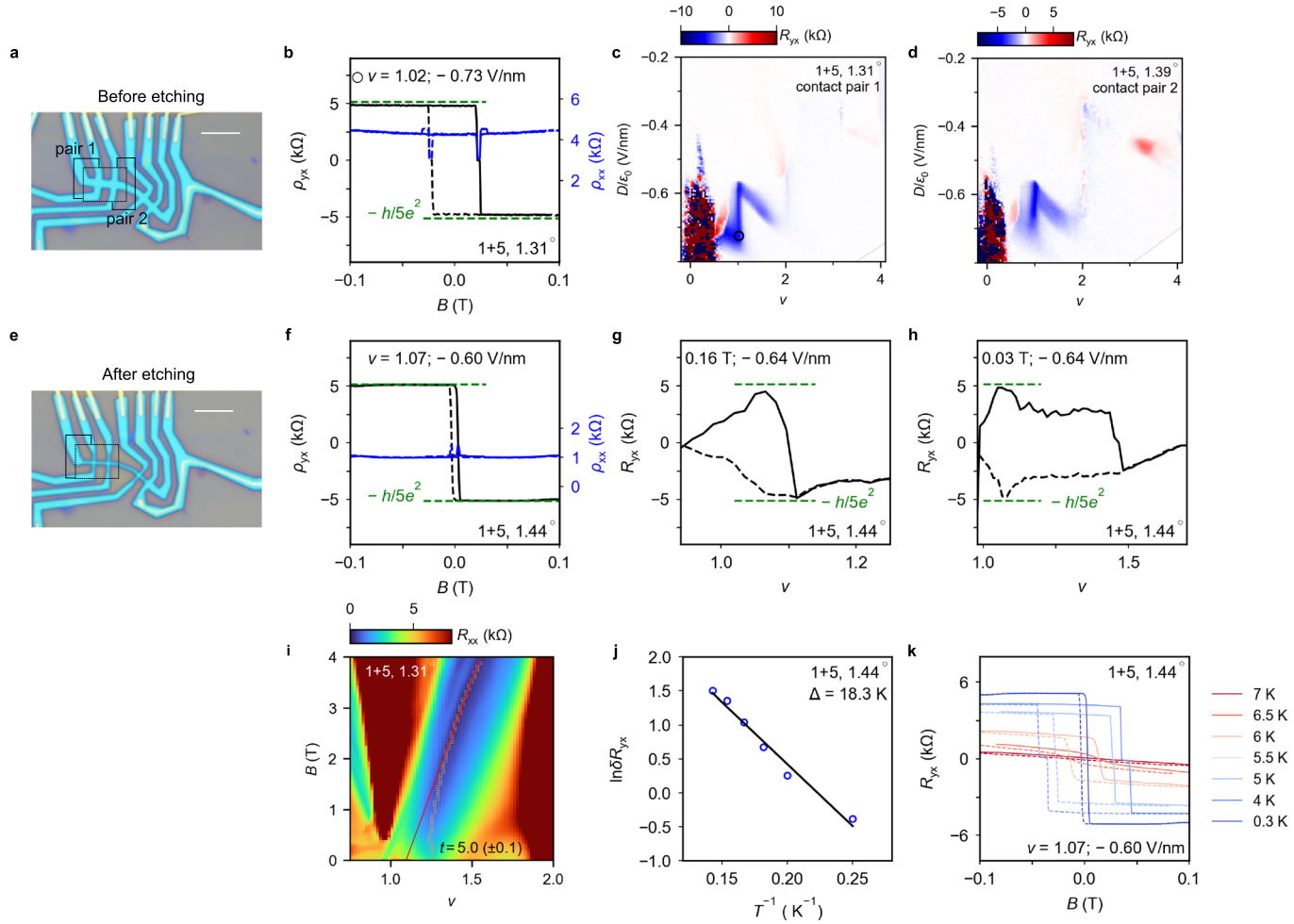

Extended Data Fig. 4 | (1+5) graphene device before and after etching. **a**-**d**, Before etching. **a**, Optical micrograph of the device before etching. Scale bar, 5 μm. **b**, ρ_{yx} and ρ_{xx} measured as a function of B (corresponding point labeled in c). **c**,**d**, R_{yx} as a function of ν and D/ε_0 for two contact pairs before etching. $B = 0.06$ T. **e**-**j**, After etching. **e**, Optical micrograph of the device after etching. The contact pair used for measuring R_{yx} in the 1.44°-(1+5) device is indicated. Scale bar, 5 μm. **f**, ρ_{yx} and ρ_{xx} measured as a function of B around $\nu = 1$. R_{yx} and R_{xx} data are shown in main Fig. 3f. **g**,**h**, Doping-induced switching of high-Chern-number magnetization. Data over a more complete magnetic-field range are shown in main Fig. 4f. $T = 0.05$ K. **i**, R_{xx} as a function of ν and B for the 1.31°-(1+5) device. $D/\varepsilon_0 = -0.66$ V/nm. The red solid line is a linear fit to the hollow circles, which mark ν for the local extremum at each B. Data above 2 T, where a clear slope begins to develop, are used for fitting. **j**, Deviation of R_{yx} from quantization plotted as a function of temperature, extracting a gap size $\Delta = 18.3$ K for the 1.44°-(1+5) device by fitting $\delta R_{yx} = \exp(-\Delta/k_B T)$. **k**, R_{yx} measured as a function of B at different temperatures. Solid (dashed) lines denote forward (backward) sweeps in the hysteretic plots.